Superlubricity in Solid Lubricated Sliding and Rolling Contacts

Ali Zayaan Macknojia[†], Mohammad Eskandari[†], Khalil Omotosho[†], Maria Cinta Lorenzo Martin[‡], Aditya Ayyagari[*†], and Diana Berman[*,†]

[†]*Department of Materials Science and Engineering, The University of North Texas, Denton, Texas, USA, 76201*

[‡]*Interfacial Mechanics and Materials Group, Applied Materials Division, Argonne National Laboratory, Lemont, IL, USA, 60439*

Abstract

Superlubricity, or near zero friction is a highly desired lubrication state for a wide range of practical applications. Although such application scenarios often involve complex contact geometries, solid lubricant technologies, including previous efforts on achieving superlubricity, are almost entirely in linear sliding test conditions. This report demonstrates an experimental pathway to yield superlubricity in rolling-sliding contact conditions using solid-lubricant materials. Ti_3C_2X based solid lubricant was tested under complex sliding-rolling conditions at engineering-significant contact pressures. The material's compression and inter-layer shearing result in material reconstruction to pose superlubricity. High-resolution transmission electron microscopy analysis, complemented by multi-scan Raman spectroscopy showed the formation of a robust amorphous tribolayer. This demonstration is expected to not only advance the applied aspects in the development of oil-free solid lubricants but also push the boundaries of fundamental understanding of materials' structure-property relations across physical states.

Introduction

Organic, synthetic, and mineral oils are traditionally used for wear and friction reduction in mechanical components, especially those experiencing various rolling/sliding regimes.[1,2] However, their use is not always feasible due to environmental limitations such as vacuum or high temperature, or restrictions imposed by the applications, such as in aerospace, pharmaceutical, or food industries. Challenges also arise due to the large volume of lubricants required and the associated risks of cross-contamination.

Solid lubricant materials provide an alternative approach to lubrication by supplying the protective material directly to the sliding interface. This separates the chemically active contacting surfaces, forming a tribolayer that passivates the surface by saturating the dangling bonds, and in

some cases reducing the area of contact.[3–8] Among the solid lubricant materials, the most promising ones are layered, or two-dimensional (2D), structures. Graphite and MoS_2, mostly in their bulk forms, have been used for friction and wear reduction of sliding components for decades.[9–11] The demonstration of the excellent tribological potential of graphene in single or few-layer form[12] accelerated the work in 2D tribology and led to the implementation of 2D lubricants across various scales and conditions.[13] Moreover, the use of graphene enabled achieving macroscale superlubricity regime,[10] the state of vanishing friction, highly desirable from the materials sustainability and energy efficiency standpoints.[14] The superlubricity was successfully achieved with other systems, such as MoS_2, MXene, and black phosphorous.[9] However, one significant detail is that those studies were performed for sliding conditions which significantly limit the implementation of solid lubricants.

For complex geometry applications such as in rolling, rolling-sliding, and combinations thereof, a major part of the work is done with various lubricating oils.[15–21] Such analysis is performed on a standardized test rig developed to study the friction response under sliding rolling conditions is the miniature traction machine (MTM). This test rig mimics the contact conditions in gears of various types of configurations, and hence offers scope for robust characterization of the lubricant materials. Though oil lubrication systems can yield low friction, achieving superlubricity in MTM systems remains rather elusive.

This study adopted the MTM platform to study and gain an overarching understanding of whether solid lubricant materials can be designed to work in conditions beyond pure sliding, enabling superlubricity under rolling conditions. For this, MXene-MoS_2 lubricant, previously reported to sustain superlubricity under high load and sliding speed conditions, has been employed.[22] The study demonstrated that the superlubricity regime can be adapted to sliding-rolling conditions as well. A detailed analysis with varying load, speed, and slide-to-roll ratio was carried out to probe the lubrication efficiency of MXene-MoS_2 lubricant and unravel the structural and chemical modifications when the rolling moving component is introduced. Optical profilometry, electron microscopy, Raman and X-ray photoelectron spectroscopy, and nanoindentation were used to understand the phenomenon that produced the lubricity properties.

Materials and Methods

***Materials*:** Weighed proportions of Ti_3C_2X and MoS_2 were added to a carrier solution (ethanol) and spray coated onto heated (80 ^oC) steel substrates (46 mm diameter hardened and tempered AISI52100 steel disc with a maximum hardness of 59 HR_c and surface roughness of $R_a \approx 215 \pm 20$ nm). Pristine micro-crystalline MXene ($Ti_3C_2T_x$) (~100 nm in diameter flakes, obtained from Nanochemazone, Leduc, Alberta, Canada), and MoS_2 (~90 nm in diameter flakes, obtained from Graphene Laboratories Inc, Ronkonkoma, NY, USA) powders were added to the ethanol, sonicated, and tumbled. These MXene and MoS_2 powders were mixed in 23:77 ratio respectively and deposited using a pneumatic spray setup. Additional details on the composition matrix and optimization framework of the solid lubricant are presented elsewhere.[22]

Deposition: The carrier solution bearing the solid lubricants was spray deposited onto a heated steel MTM disc. A uniform dispersion rate and pass-to-pass delay were tuned such that the ethanol immediately evaporated upon contacting the hot surface, effectively transferring the solid lubricant materials.

Characterization: The thickness of the spray-deposited solid lubricant coating was measured using the Filmetrics Profilm3D Optical Profilometer (KLA Instruments, Milpitas, CA, USA). KLI Instruments Nanoindentation test platform was used to measure the mechanical properties of the coating and tribolayer. X-ray photoelectron spectroscopy was performed using PHI Versaprobe, Al K_α radiation. The morphological details were captured using a Hitachi TM 3000 tabletop scanning electron microscope (SEM), and JEOL JEM-2100F Field Emission-Gun Transmission Electron Microscope (TEM) was used to capture the transmission electron micrographs. Chemical changes in the coatings were recorded using Raman spectroscopy (Renishaw Raman system with a green 532 nm wavelength laser).

***Description of modified MTM setup*:** The standard MTM (PCS Instruments, London, UK) was modified as shown in Figure 1. The oil reservoir of the MTM unit was emptied, rinsed with organic solvents, wiped clean, and dried. A nitrogen line was connected to the oil outlet spout, effectively creating a controlled environment sample chamber. The contact pressures were calculated using Equation 1 and Equation 2, where W is the applied load; D is the diameter of the ball (19.05 mm, or 0.75 inch, with a surface roughness of $R_a \approx 25$ nm); E^* is the reduced elastic

modulus; and E_1, E_2, ν_1, ν_2 are the elastic moduli (~ 190GPa) and Poisson's ratios (0.27-0.3) of the AISI 52100 steel (ball and substrate material) respectively.

$$p_{max} = \left(\frac{1}{\pi}\right)\left(\frac{24 \cdot W \cdot E^{*2}}{D^2}\right)^{\frac{1}{3}} \quad (1)$$

$$\frac{1}{E^*} = \left(\frac{1-\nu_1^2}{E_1}\right) + \left(\frac{1-\nu_2^2}{E_2}\right) \quad (2)$$

The prepared samples were assembled in the test chamber, top cover placed and locked, and subsequently purged with pure, dry nitrogen at a rate of 0.5 centiliters per minute for a minimum of 30 min before the onset of the test and through the entire test duration. Although the chamber itself was not a perfect seal, the continuous supply of nitrogen was sufficient to prevent ambient air back-flow into the sample chamber. The slide-to-roll ratio (SRR) was calculated using Equation 3.

$$SRR = 100\% * \left(\frac{\left|Velocity_{Sliding}\right|}{Veolcity_{Entrainment}}\right)$$

$$= 100\% * \left(\frac{|V_{Ball} - V_{Disc}|}{\frac{V_{Ball} + V_{Disc}}{2}}\right) \quad (3)$$

An extensive exploratory study was performed on the solid lubricated samples at various test conditions. The first proof-of-concept demonstration experiment was performed at a nominal load of 10 N, 100 mm/s, and 5% slide-to-roll ratio. Based on the result of this low-load, low-speed experiment a larger test matrix consisting of higher contact pressures and more severe sliding conditions was planned. These tests were performed at 20 N, an initial sliding speed of 100 mm/s, and a slide-to-roll ratio spanning from 200% to 5%. Finally, an endurance test was conducted at 30 N, 500 mm/s, and 5% SRR. Post-test characterization and analysis of mechanical properties were performed to unravel the material's transformation during the tests.

Results

Lubricant preparation and deposition

The MXene-MoS_2 mixture was spray-coated on rough steel surfaces and analyzed under sliding/rolling conditions, as shown in **Figure 1**. The scanning electron microscope images of the starting materials before dispersion into the carrier liquid are shown in **Figure 1a** for the MXene

powder and in **Figure 1b** for the MoS_2 powder. The MXene flakes had an accordion-like multilayer morphology, with an average flake size of 25 ± 7 μm, whereas the average flake diameter of the MoS_2 flakes was 500 ± 100 nm and appeared larger in the SEM image due to agglomeration. A photograph of the suspension is shown in **Figure 1c**. The materials remained in the suspension without lumping or displaying segregation. A cartoon showing the deposition process on the MTM disc is shown in **Figure 1d**. After the deposition of the coating, a sharp step through the deposit was created using a diamond scribe, and the step height between the substrate and the top of the coating was measured as coating thickness. The average coating thickness and roughness were 2.5 ± 0.15 μm and 137 ± 50 nm, respectively (shown in Supplemental Information **Figure S1**). The experimental setup of the MTM instrument with the sample disc and ball assembled is shown in **Figure 1e**.

Tribological characterization

The coatings were assessed for their friction and wear characteristics in the MTM setup (**Figure 2**).

Table 1: *Summary of parametric studies performed in the MTM experimental setup.*

Test	Load (N)	Velocity (mm/s)	SRR (%)	Friction (μ)
Test 1 Proof of Concept	10	100	5	0.0421
Test 2 Step 1	20	100	200	0.0190
Test 2 Step 2	20	100	150	0.0161
Test 2 Step 3	20	100	100	0.0150
Test 2 Step 4	20	100	50	0.0143
Test 2 Step 5	20	100	25	0.0140
Test 2 Step 6	20	100	5	0.0130
Test 3 Endurance Test	30	500	5	0.0054
Test 4 PAO-10 (Reference)	30	500	5	0.254

The friction data from the exploratory studies is shown in **Figure 2a** and the values are presented in **Table 1**. The 3D plot shows the effect of the sliding velocity of the disc, normal load, and resulting coefficient of friction. The plot shows the friction coefficient below 0.5 for all tested conditions. For reference, the steel substrate tested with PAO-10 oil under similar conditions

yielded a friction coefficient of 0.254. Next, the coating was tested across the full range of SRR values. The full frictiograms of the SRR variation test with progressively increasing rolling contribution are shown in **Figure 2b**. At 200% SRR, the disc rotates with a speed of 200 mm/s with the ball remaining stationary (0 mm/s), mimicking a typical pure sliding ball-on-disc set-up, whereas, at 5% SRR, these values were 102.55 mm/s and 97.55 mm/s, respectively. The friction was observed to decrease from 200% SRR to 5% SRR. The friction coefficient at the end at 200% SRR was 0.0190, at the end of 150% SRR step was 0.0161, at the end of 100% SRR step was 0.0150, at the end of 50% SRR step was 0.0143, at the end of 25% SRR step was 0.140, and at the end of 5% SRR step was 0.013. While these friction results were very low, they did not yield superlubricity, when friction should drop below 0.01. Prior studies demonstrated that MXene-MoS_2 lubricant is very sensitive to applied load conditions.[22] Therefore, to achieve superlubricity, the applied contact pressure was increased to 1 GPa (30 N) while testing at a constant 5% SRR (**Figure 2c**). This test corresponds to the highest contact pressure, rolling contribution, and sliding velocity condition in the current study. Under these conditions, the ball's rotation speed is 487 mm/s, and the disc's sliding speed is 512 mm/s, producing the desired slide-to-roll ratio of 5%. Indeed, the steady-state friction dropped to 0.0054 for a prolonged duration during the experiment. Notably, in comparison to the 2D material providing superlubricity, the uncoated steel-on-steel contact demonstrated a high friction of 0.78 that caused immediate failure of the MTM test, while the use of a commercially available PAO-10 base oil reduced friction to only 0.254 under the same testing conditions (**Figure 2c**). This result implies that solid lubricant materials are not only limited to being used in sliding conditions but also under sliding-rolling conditions across different contact conditions. The observed friction values are comparable with other state-of-the-art solid lubricant materials that show a classical, linear, monotonous change in friction with sliding speed or normal load.[9–11,22–31]

The wear on the tracks from the two tests was quantified. **Figure 2d** shows the line profiles of the wear tracks at 20 N and 100 mm/s initial velocity and the 30 N and 500 mm/s initial velocity experiment. The blue dashed line shows the substrate and coating interface in purple. The line profile indicates that the entire wear is contained within the coating, and no wear loss occurred across the through-thickness of the deposit, i.e., coating did not rupture exposing the substrate steel. This means that considerable the service life remained on the deposit (as confirmed by SEM-EDS elemental map, Supplemental Information, Figure S2).

Materials characterization

The materials characterization was performed before and after the tests to quantify the changes and understand the mechanisms at play. The Raman Spectra were acquired from the two contacting bodies. The Raman spectra from the disc are shown in **Figure 3**. A photograph of the disc loaded into the analysis chamber of the Raman Spectrometer is shown in **Figure 3a**, with the two sliding tracks visible on the sample substrate. The spectra from the as-deposited coating are shown in **Figure 3b**. The signature of the materials from the two separate tests was similar and the representative line graph is shown in **Figure 3c**, and a 2D area scan across the wear track is shown in **Figure 3d**. When the test was carried out under a nitrogen atmosphere, no deleterious intercalation with oxygen or structural water was seen in either of the wear tracks. The peak positions and intensities remained fairly unchanged. Importantly, peaks at 159, 666, and 820 cm^{-1} that correspond to MoO_3 were absent.[32] The absence of oxide peaks was also confirmed using XPS analysis (Full spectra presented in Supplemental Information, Figure S3). The inside of the sliding path showed a strong signal emanating from the A_{1g} lattice vibration and all other peak positions were present on the as-deposited coating, outside the wear tracks. This shows that crystal plane reorientation occurred to favor the basal plane alignment normal to the loading axis.

The Raman spectra acquired from the counterface ball are shown in **Figure 3e-h**. A schematic of the ball contact region is shown in **Figure 3e**, and the corresponding contact area's while light image is shown in Figure 3h. There are two distinct regions, namely the center of the contact region (blue) where peak contact stress is experienced by the counterface, and the region adjacent to the peak stress portion where contact with a pile-up of the solid lubricant transferred from the disc seems to be still intact, shown in red. The Raman signature from the pile-up region is shown in **Figure 3f** and that of the peak contact-stress region is shown in **Figure 3g**. The area map of the entire region of interest is shown in **Figure 3h**. In contrast to the solid lubricant material deposited on the disc, and the off-set region, the spectra indicated significant material change. The intensity and shapes of the characteristic peaks were diminished and distorted, indicating the transfer layer was composed of pulverized or disintegrated material, with some resemblance to the starting materials.

A small extract from the foregoing transfer layer was placed on a TEM copper grid for further analysis of the microstructure and chemical composition. The resulting transmission electron

micrographs are shown in **Figure 4**. The bright field image of the transfer layer, the selected area electron diffraction (SAED) image, and TEM EDS elemental maps are shown. The bright field image did not contain any lattice fringes or crystalline features indicating it to be amorphous. The SAED pattern confirmed this observation as being completely devoid of any periodic lattice features, as evidenced by the smeared halo. The constituent elements from the starting materials, namely, Mo, S, and Ti, C, were present. The TEM observation corroborates with the distorted Raman Spectra shown in Figure 3g-h.

Discussion

The data presented thus far, namely the friction graphs, minimal wear loss, materials characterization carried out using Raman Spectroscopy on the ball and disc, and TEM imaging and EDS point toward the robustness of the solid lubricant containing MoS_2 and MXene in rolling-sliding. The improvement in lubricity performance of the material when moving from pure sliding which is 200% SRR to increased rolling component, which is 5% SRR is attributed to multiple factors. Increasing the ball speed while simultaneously decreasing the disc speed results in an increase in the slide-to-roll ratio as shown in Equation 3. These contact conditions result in progressively increasing shearing stresses in the lubricant material. The friction response from the lubricant is dependent on the materials' shear strength, and ability to withstand the normal and shear stresses. From the data presented, it is evident that the lubricant can withstand high loads and shear stresses and responds by producing greater slip in the inter-planar and trans-crystalline systems resulting in increased lubricity, as reflected in the decreasing friction plot shown in Figure 2a. This is possible as the principal shear force accommodation is provided by the MoS_2 flakes, while the MXene provides the necessary mechanical strength in addition to shearing from the MXene itself. Secondly, with prolonged sliding, and increasing the normal load, the number density of the asperities on the surface decreases and promotes re-orientation of the basal planes that enables inter-layer slip and intra-crystal shear.[33–41]

It has been previously shown that the hardness of the tribolayer is considerably high compared to the as-deposited material due to the compaction and sliding, that holds in this case. The hardness and the elastic modulus of the as-deposited coating material were 1001 ± 10 MPa and 5557 ± 100 MPa, respectively, whereas the hardness and the elastic modulus of the compacted tribolayer material increased to 2250 ± 20 MPa and 8873 ± 120 MPa, respectively (as shown in Supplemental

Information Figure S4). Finally, the material integrity both in the form of retaining a high structural integrity in the surface and sub-surface layers on the disc and forming an inert amorphous transfer layer on the ball facilitates the lubricity behavior. The formation of an amorphous transfer layer on the counterface ball contrasts with our previous report where no such morphological changes were seen.[22] This difference arises due to the variation in the contact conditions between the two experimental setups used in the two studies. In the classical pin-on-disc study, the ball remains stationary and therefore the experiment is in pure sliding contact. The transfer layer formed on the ball is in a quasi-stable state and does not change unless there is an excessive pile-up and dislodging of material. Due to the nature of the pure sliding experiment shearing experienced at the interface of the stationary ball and the sliding disc is much lower compared to a sliding-rolling experiment. In the current case, the ball rotates around its axis, in addition to the disc's sliding motion, producing higher shear, and a continuous fresh surface is made available for the material transformation. Since both the ball and disc are in relative motion, there is a greater shear experienced at the contact that provides the activation energy for the vitrification of the crystalline structure. Similar results of shear-induced vitrification and phase changes of crystalline materials are also seen in other material systems.[42–46] Previous studies successfully demonstrated ultralow friction behavior for a range of solid lubricant materials, including diamond-like carbon (DLC), molybdenum disulfide (MoS2), and graphene, [66-68] though only under sliding conditions. The current study shows that the MoS_2 and $Ti_3C_2T_x$ materials' combination has demonstrated the viability of using properly designed solid lubricants not only in sliding but also in sliding-rolling conditions, with friction performance at least as good as oil-based lubricants as shown in **Figure 5**.

In conclusion, it is demonstrated without any ambiguity that solid lubricant materials have reached a high technology readiness level for applications in not only sliding but also with simultaneous rolling components, as high as 100%, albeit with careful selection and processing of materials. This study shows that multi-layer micro-crystalline materials undergo shear (or slip) that renders prolonged and reliable lubricity under moderate to high contact pressures. This demonstration advances the state-of-the-art of solid-lubrication science into complex contact condition mechanics and thereby opens pathways for complex multifarious applications.

Acknowledgment

The authors acknowledge the support of this work by the National Science Foundation (NSF) (Award No. 2323452). The use of the Center for Nanoscale Materials, an Office of Science user facility, was supported by the U.S. Department of Energy, Office of Science, Office of Basic Energy Sciences, and Division of Chemical Sciences, Geosciences, and Biosciences; and Office of Energy Efficiency and Renewable Energy, Vehicle Technologies and Advanced Manufacturing Offices under Contract No. DE-AC0206CH-11357.

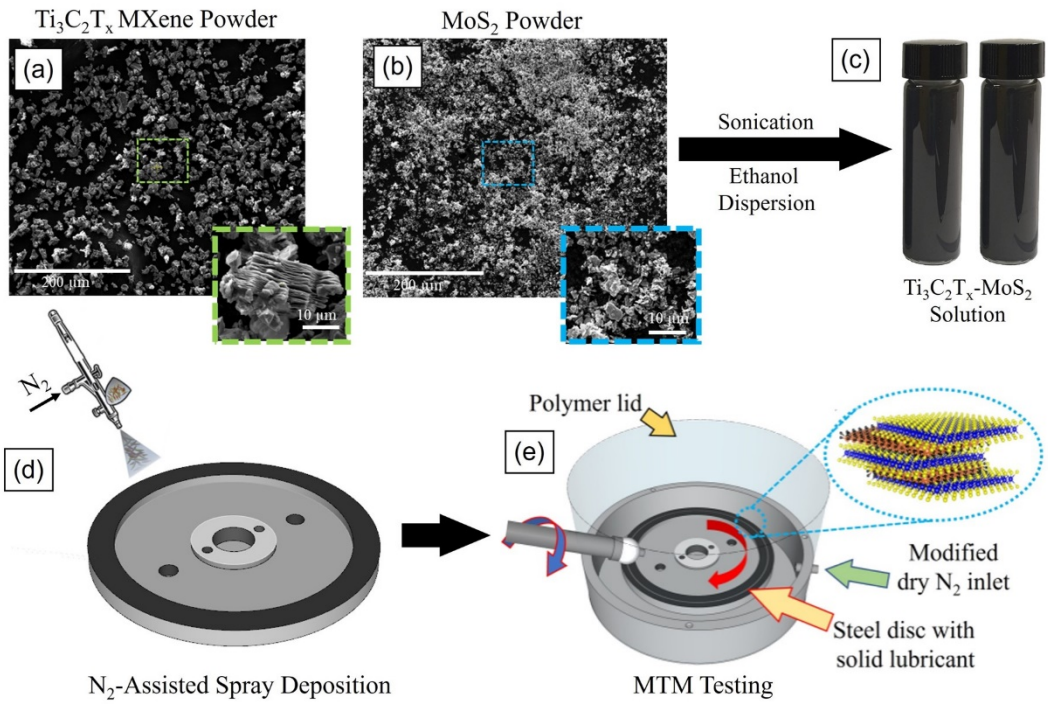

Figure 1: *Scanning electron microscope image of (a) Ti_3C_2X MXene powder and an inset showing a high magnification image showing the accordion-like structure, (b) MoS_2 powder and inset showing a high magnification image, (c) Suspension containing well dispersed solid materials (d) A cartoon showing the deposition process using nitrogen assisted spray coating, and (e) schematic showing the modified MTM machine setup with nitrogen line connected to the test chamber.*

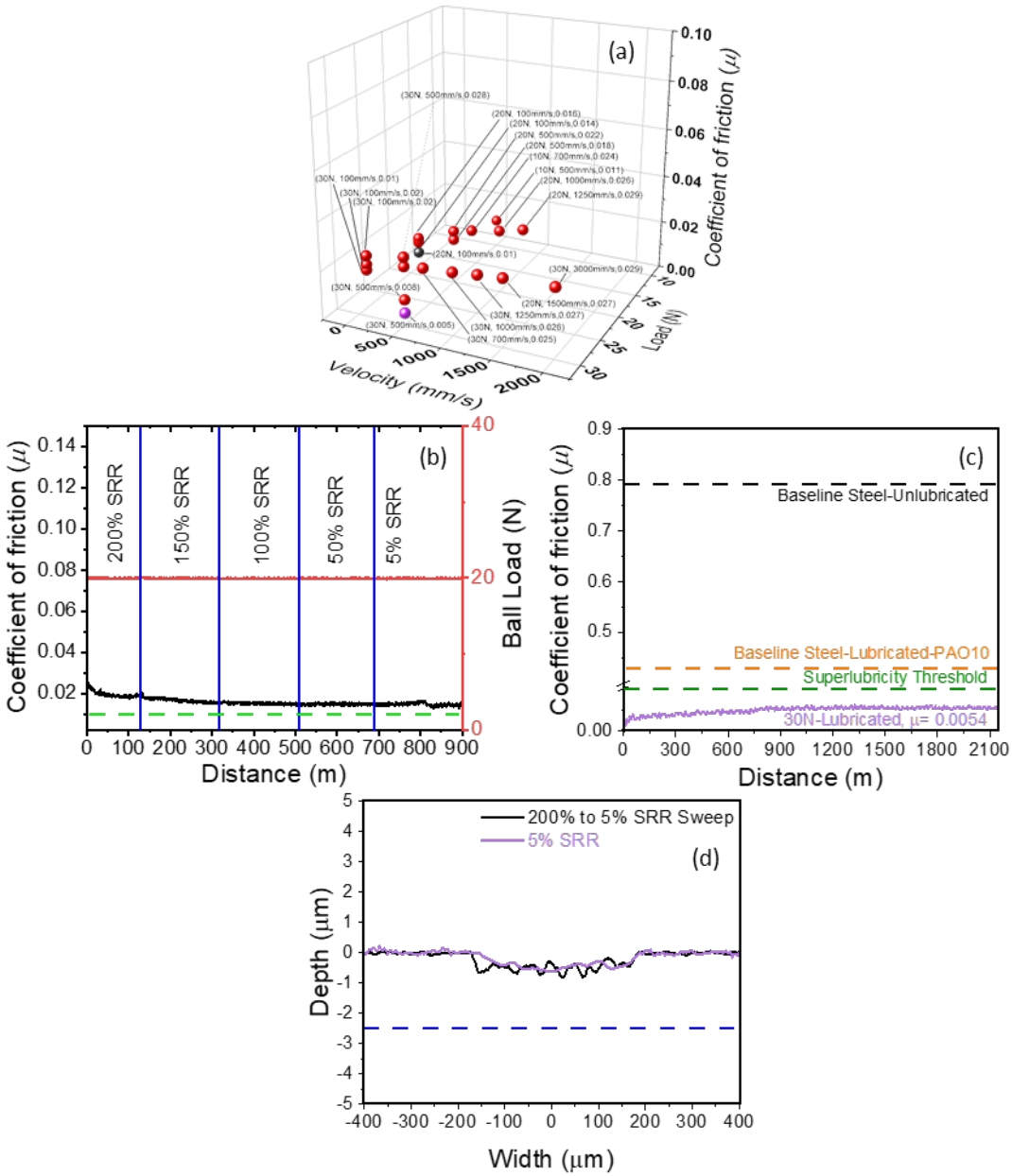

Figure 2: *(a) Summary of friction data recorded at various velocity and load conditions (specific conditions and the corresponding stable COF values are included next to the data points). The results further reported in (b) and (c) with the lowest observed friction data are highlighted in purple (30 N, 500 mm/s, 5% SRR) and grey (SRR sweep from 200 % to 5 % at 20 N), correspondingly. (b) The friction data observed at 20 N normal load, corresponding to 875.2 MPa, under the continuous sweep of SRR from 200% to 5%. (c) The friction data observed at 30 N normal load, corresponding to 1001 MPa, tested at 5% SRR, and constant disc speed of 512.39 mm/s, and a ball speed of 487.36 mm/s, corresponding to 5% SRR. (d) Line profiles of the wear tracks continuous SRR sweep experiments, at 20 N and 100 mm/s initial velocity and 30 N and 500 mm/s initial velocity experiment. The blue dashed line shows the substrate and coating interface indicating that the entire deformation seen as the wear track is contained within the materials deposit, and no wear loss occurred on the substrate steel.*

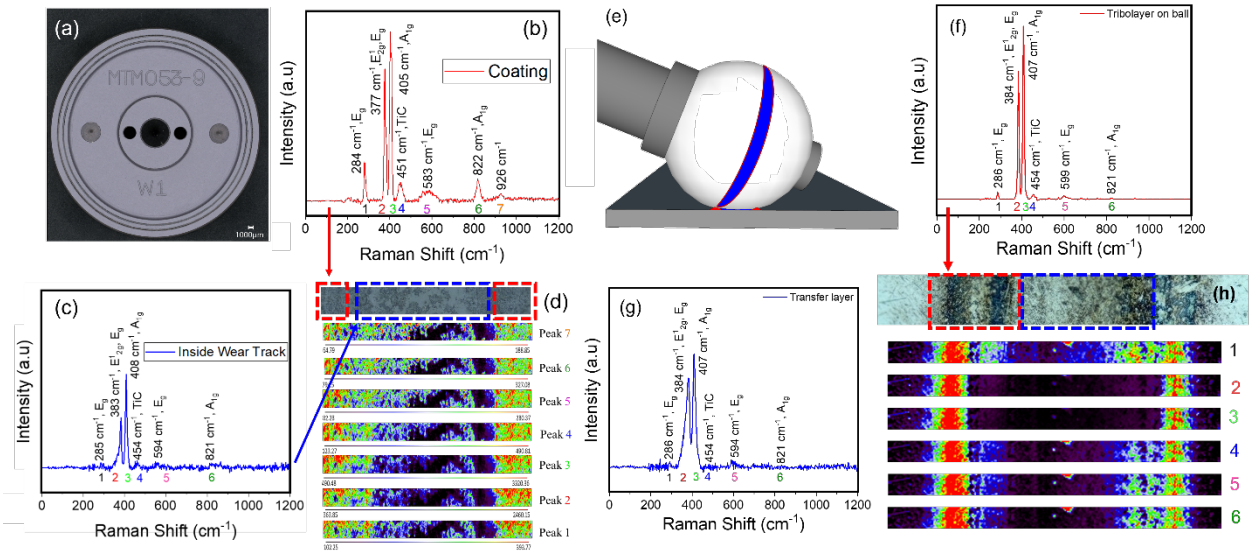

Figure 3: *(a) A photograph of the disc loaded into the analysis chamber of the Raman Spectrometer. (b) The Raman spectra from the as-deposited coating showing peaks corresponding to the MoS_2 and MXene materials. (c) Representative 1D line spectral plot showing the signature from the sliding path (d) 2D Raman area mapping of the wear track captured from the 1 GPa sliding experiment. (e) A 3D schematic of the counterbody used was loaded into the analysis chamber of the Raman Spectrometer. (f) The Raman spectra from the tribolayer formed on ball showing peaks corresponding to the MoS_2 and MXene materials. (g) Representative 1D line spectral plot showing the signature from the transfer layer on ball (h) 2D Raman area mapping of the wear track captured from the 1 GPa sliding experiment.*

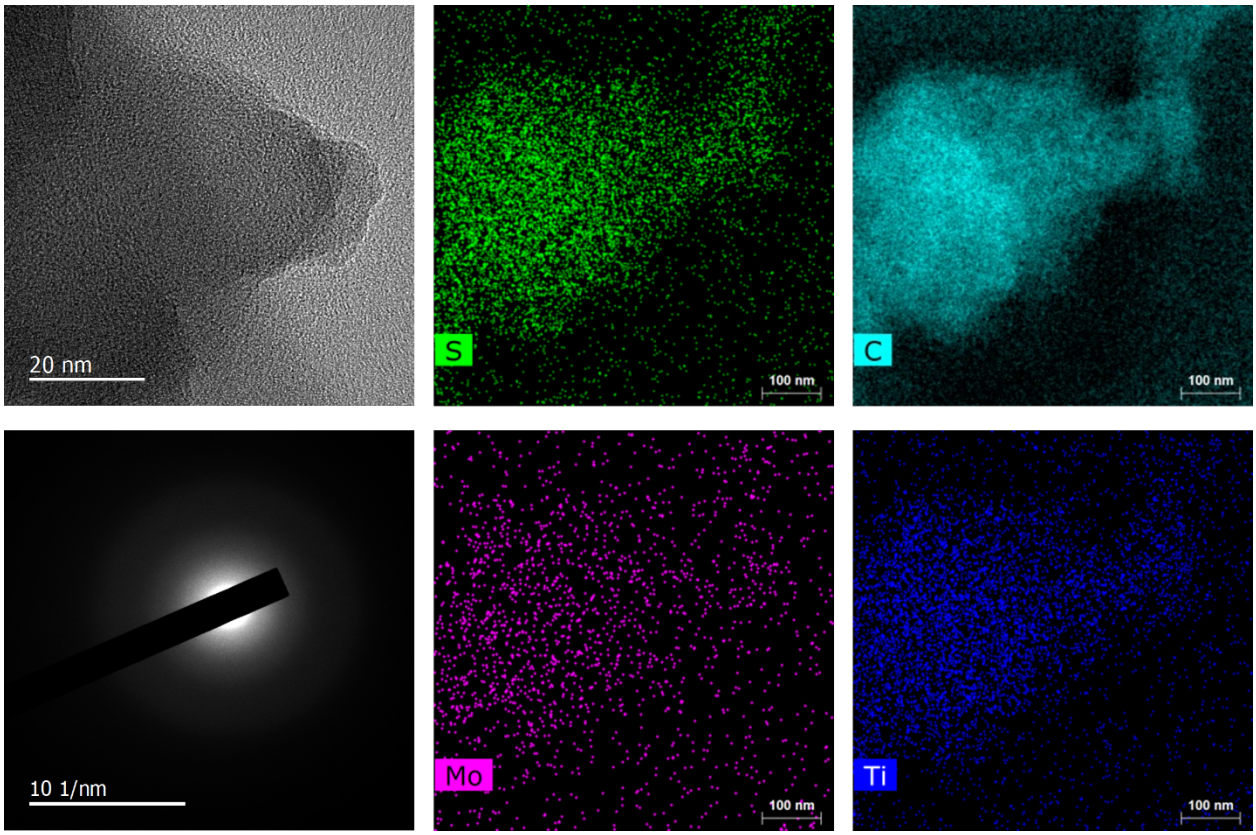

Figure 4: *Bright field transmission electron image showing the shear-induced structural changes in the tribolayer being devoid of the lattice structure. The electron diffraction images showing an amorphous phase halo and the corresponding TEM-EDS image showing a uniform distribution of constituent elements in the entire sample.*

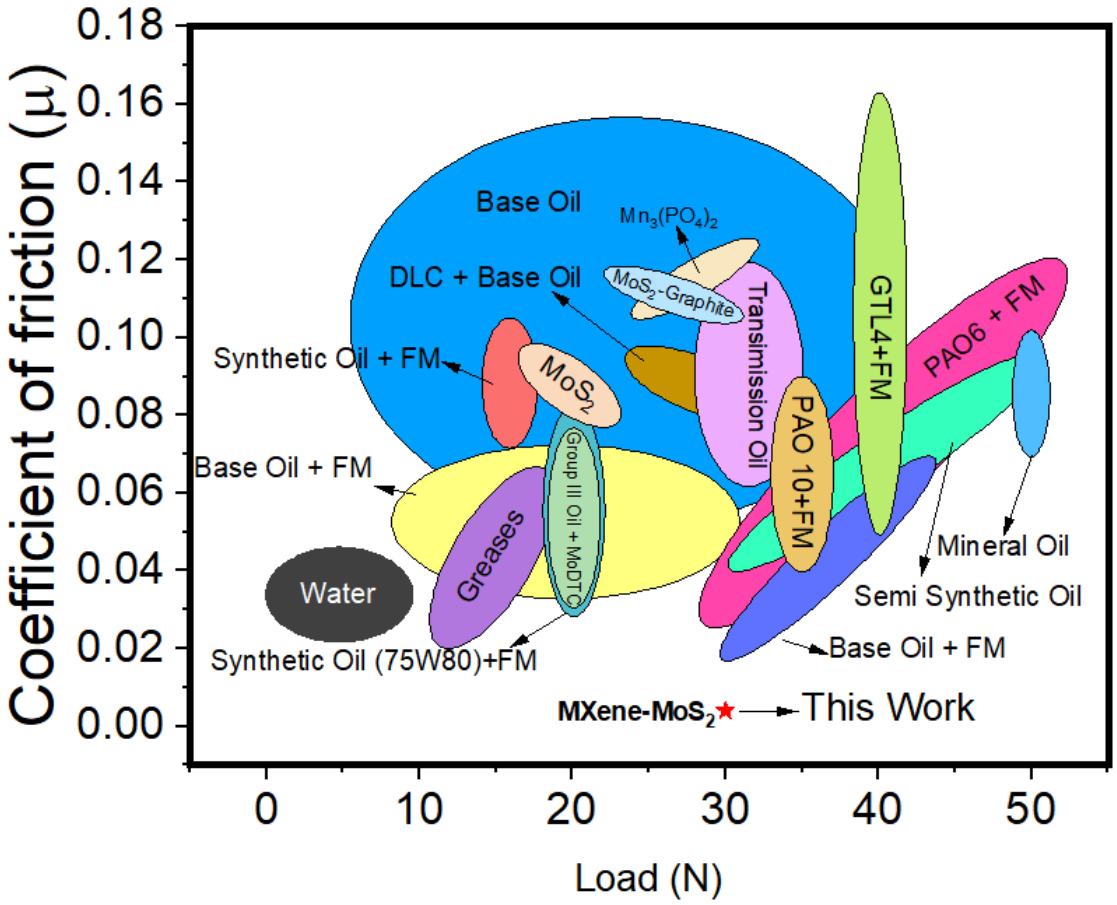

Figure 5: *State-of-the-art lubricants' properties plotted on an Ashby chart type plot*[16–19,47–65]

Figure Captions

Figure 1: *Scanning electron microscope image of (a) Ti_3C_2X MXene powder and an inset showing a high magnification image showing the accordion-like structure, (b) MoS_2 powder and inset showing a high magnification image, (c) Suspension containing well dispersed solid materials (d) A cartoon showing the deposition process using nitrogen assisted spray coating, and (e) Schematic showing the modified MTM machine setup with nitrogen line connected to the test chamber*

Figure 2: *(a) Summary of friction data recorded at various velocity and load conditions (specific conditions and the corresponding stable COF values are included next to the data points). The results further reported in (b) and (c) with the lowest observed friction data are highlighted in purple (30 N, 500 mm/s, 5% SRR) and grey (SRR sweep from 200 % to 5 % at 20 N), correspondingly. (b) The friction data observed at 20 N normal load, corresponding to 875.2 MPa, under the continuous sweep of SRR from 200% to 5%. (c) The friction data observed at 30 N normal load, corresponding to 1001 MPa, tested at 5% SRR, and constant disc speed of 512.39 mm/s, and a ball speed of 487.36 mm/s, corresponding to 5% SRR. (d) Line profiles of the wear tracks continuous SRR sweep experiments, at 20 N and 100 mm/s initial velocity and 30 N and 500 mm/s initial velocity experiment. The blue dashed line shows the substrate and coating interface indicating that the entire deformation seen as the wear track is contained within the materials deposit, and no wear loss occurred on the substrate steel.*

Figure 3: *(a) A photograph of the disc loaded into the analysis chamber of the Raman Spectrometer. (b) The Raman spectra from the as-deposited coating showing peaks corresponding to the MoS_2 and MXene materials. (c) Representative 1D line spectral plot showing the signature from the sliding path (d) 2D Raman area mapping of the wear track captured from the 1 GPa sliding experiment. (a) A photograph of the disc loaded into the analysis chamber of the Raman Spectrometer. (b) The Raman spectra from the deposited coating showing peaks corresponding to the MoS_2 and MXene materials. (c) Representative 1D line spectral plot showing the signature from the sliding path (d) 2D Raman area mapping of the wear track captured from the 1 GPa sliding experiment.*

Figure 4: *Bright field transmission electron image showing the shear-induced structural changes in the tribolayer being devoid of the lattice structure. The electron diffraction images showing an amorphous phase halo and the corresponding TEM-EDS image showing a uniform distribution of constituent elements in the entire sample.*

Figure 5: *State-of-the-art lubricants' properties plotted on an Ashby chart type plot*[16–19,47–65]

References

(1) Lu, X.; Khonsari, M.; Gelinck, E. The Stribeck curve: experimental results and theoretical prediction. *Journal of tribology* **2006**, *128*, 789–794.

(2) Woydt, M.; Wasche, R. The history of the Stribeck curve and ball bearing steels: The role of Adolf Martens. *Wear* **2010**, *268*, 1542–1546.

(3) Donnet, C.; Erdemir, A. Solid lubricant coatings: recent developments and future trends. *Tribology letters* **2004**, *17*, 389–397.

(4) Teer, D. New solid lubricant coatings. *Wear* **2001**, *251*, 1068–1074.

(5) Sunil, T.; Sandeep, M.; Kumaraswami, R.; Shravan, A. A critical review on solid lubricants. *Int. J. Mech. Eng. Technol* **2016**, *7*, 193–199.

(6) Singer, I. Solid lubrication processes. *Fundamentals of friction: macroscopic and microscopic processes* **1992**, 237–261.

(7) Miyoshi, K. *Solid lubrication fundamentals and applications*; CRC Press, 2019.

(8) Kumar, R.; Banga, H. K.; Singh, H.; Kundal, S. An outline on modern day applications of solid lubricants. *Materials Today: Proceedings* **2020**, *28*, 1962–1967.

(9) Ayyagari, A.; Alam, K. I.; Berman, D.; Erdemir, A. Progress in superlubricity across different media and material systems—a review. *Frontiers in Mechanical Engineering* **2022**, *8*.

(10) Berman, D.; Deshmukh, S. A.; Sankaranarayanan, S. K.; Erdemir, A.; Sumant, A. V. Macroscale superlubricity enabled by graphene nanoscroll formation. *Science* **2015**, *348*, 1118–1122.

(11) Berman, D.; Mutyala, K. C.; Srinivasan, S.; Sankaranarayanan, S. K.; Erdemir, A.; Shevchenko, E. V.; Sumant, A. V. Iron-Nanoparticle Driven Tribochemistry Leading to Superlubric Sliding Interfaces. *Advanced Materials Interfaces* **2019**, *6*, 1901416.

(12) Berman, D.; Erdemir, A.; Sumant, A. V. Graphene: a new emerging lubricant. *Materials today* **2014**, *17*, 31–42.

(13) Marian, M.; Berman, D.; Rota, A.; Jackson, R. L.; Rosenkranz, A. Layered 2D nanomaterials to tailor friction and wear in machine elements—A review. *Advanced Materials Interfaces* **2022**, *9*, 2101622.

(14) Berman, D.; Erdemir, A.; Sumant, A. V. Approaches for achieving superlubricity in two-dimensional materials. *ACS Nano* **2018**, *12*, 2122–2137.

(15) Müller, M.; Lee, S.; Spikes, H. A.; Spencer, N. D. The influence of molecular architecture on the macroscopic lubrication properties of the brush-like co-polyelectrolyte poly (L-lysine)-g-poly (ethylene glycol)(PLL-g-PEG) adsorbed on oxide surfaces. *Tribology Letters* **2003**, *15*, 395–405.

(16) Vengudusamy, B.; Grafl, A.; Novotny-Farkas, F.; Schöfmann, W. Comparison of frictional properties of gear oils in boundary and mixed lubricated rolling–sliding and pure sliding contacts. *Tribology International* **2013**, *62*, 100–109.

(17) Balarini, R.; Diniz, G.; Profito, F. J.; Souza, R. M. d. Comparison of unidirectional and reciprocating tribometers in tests with MoDTC-containing oils under boundary lubrication. *Tribology International* **2020**, *149*, 105686.

(18) García, A.; González, R.; Battez, A. H.; Viesca, J.; Monge, R.; Fernández-González, A.; Hadfield, M. Ionic liquids as a neat lubricant applied to steel–steel contacts. *Tribology International* **2014**, *72*, 42–50.

(19) Derry, M. J.; Smith, T.; O'hora, P. S.; Armes, S. P. Block copolymer nanoparticles prepared via polymerization-induced self-assembly provide excellent boundary lubrication performance for next-generation ultralow-viscosity automotive engine oils. *ACS applied materials & interfaces* **2019**, *11*, 33364–33369.

(20) Andablo-Reyes, E.; de Vicente, J.; Hidalgo-Alvarez, R.; Myant, C.; Reddyhoff, T.; Spikes, H. A. Soft elasto-hydrodynamic lubrication. *Tribology Letters* **2010**, *39*, 109– 114.

(21) Haque, T.; Korres, S.; Carey, J. T.; Jacobs, P. W.; Loos, J.; Franke, J. Lubricant effects on white etching cracking failures in thrust bearing rig tests. *Tribology Transactions* **2018**, *61*, 979–990.

(22) Macknojia, A.; Ayyagari, A.; Zambrano, D.; Rosenkranz, A.; Shevchenko, E. V.; Berman, D. Macroscale Superlubricity Induced by MXene/MoS_2 Nanocomposites on Rough Steel Surfaces under High Contact Stresses. *ACS Nano* **2023**, *17*, 2421–2430.

(23) Macknojia, A.; Ayyagari, A.; Shevchenko, E. V.; Berman, D. MXene/Graphene Oxide Nanocomposites for Friction and Wear Reduction of Rough Steel Surfaces. *Scientific Reports* **2023**,

(24) Persson, B. N. J.; Sivebæk, I. M.; Samoilov, V. N.; Zhao, K.; Volokitin, A.; Zhang, Z. On the origin of Amonton's friction law. *Journal of physics: condensed matter* **2008**, *20*, 395006.

(25) Popova, E.; Popov, V. L. The research works of Coulomb and Amonton's and generalized laws of friction. *Friction* **2015**, *3*, 183–190.

(26) Mutyala, K. C.; Singh, H.; Fouts, J. A.; Evans, R.; Doll, G. Influence of MoS_2 on the rolling contact performance of bearing steels in boundary lubrication: a different approach. *Tribology Letters* **2016**, *61*, 1–11.

(27) Mutyala, K. C.; Wu, Y. A.; Erdemir, A.; Sumant, A. V. Graphene-MoS_2 ensembles to reduce friction and wear in DLC-Steel contacts. *Carbon* **2019**, *146*, 524–527.

(28) Mutyala, K. C.; Doll, G. L.; Wen, J.; Sumant, A. V. Superlubricity in rolling/sliding contacts. *Applied Physics Letters* **2019**, *115*, 103103.

(29) Huang, S.; Mutyala, K.; Sumant, A.; Mochalin, V. Achieving superlubricity with 2D transition metal carbides (MXenes) and MXene/graphene coatings. *Materials Today Advances* **2021**, *9*, 100133.

(30) Singh, H.; Mutyala, K.; Evans, R.; Doll, G. An investigation of material and tribological properties of Sb_2O_3/Au-doped MoS_2 solid lubricant films under sliding and rolling contact in different environments. *Surface and Coatings Technology* **2015**, *284*, 281–289.

(31) Singh, H.; Mutyala, K.; Mohseni, H.; Scharf, T.; Evans, R.; Doll, G. Tribological performance and coating characteristics of sputter-deposited Ti-doped MoS_2 in rolling and sliding contact. *Tribology Transactions* **2015**, *58*, 767–777.

(32) Windom, B. C.; Sawyer, W.; Hahn, D. W. A Raman spectroscopic study of MoS 2 and MoO_3: applications to tribological systems. *Tribology Letters* **2011**, *42*, 301–310.

(33) Moser, J.; Levy, F. Crystal reorientation and wear mechanisms in MoS_2 lubricating thin films investigated by TEM. *Journal of materials research* **1993**, *8*, 206–213.

(34) Pope, L.; Panitz, J. The effects of hertzian stress and test atmosphere on the friction coefficients of MoS_2 coatings. *Surface and Coatings Technology* **1988**, *36*, 341–350.

(35) Babuska, T. F.; Curry, J. F.; Dugger, M. T.; Lu, P.; Xin, Y.; Klueter, S.; Kozen, A. C.; Grejtak, T.; Krick, B. A. Role of Environment on the Shear-Induced Structural Evolution of MoS_2 and Impact on Oxidation and Tribological Properties for Space Applications. *ACS Applied Materials & Interfaces* **2022**, *14*, 13914–13924.

(36) Curry, J. F. Friction and environmental sensitivity of molybdenum disulfide: effects of microstructure. Ph.D. thesis, Lehigh University, 2017.

(37) Curry, J. F.; Argibay, N.; Babuska, T.; Nation, B.; Martini, A.; Strandwitz, N. C.; Dugger, M. T.; Krick, B. A. Highly oriented MoS_2 coatings: tribology and environmental stability. *Tribology letters* **2016**, *64*, 1–9.

(38) Krauß, S.; Seynstahl, A.; Tremmel, S.; Meyer, B.; Bitzek, E.; Go¨ken, M.; Yokosawa, T.; Zubiri, B. A.; Spiecker, E.; Merle, B. Structural reorientation and compaction of porous MoS_2 coatings during wear testing. *Wear* **2022**, *500*, 204339.

(39) Perumal, G.; Ayyagari, A.; Chakrabarti, A.; Kannan, D.; Pati, S.; Grewal, H.; Mukherjee, S.; Singh, S.; Arora, H. Friction stir processing of stainless steel for ascertaining its superlative performance in bioimplant applications. *ACS applied materials & interfaces* **2017**, *9*, 36615–36631.

(40) Ayyagari, A. V.; Mutyala, K. C.; Sumant, A. V. Towards developing robust solid lubricant operable in multifarious environments. *Scientific Reports* **2020**, *10*, 1–12.

(41) Babuska, T.; Krick, B.; Argibay, N.; Dugger, M.; Chandross, M.; Curry, J. Revisiting the dwell effect on friction behavior of molybdenum disulfide. *Wear* **2023**, *526*, 204876.

(42) Wilking, J. N.; Mason, T. G. Irreversible shear-induced vitrification of droplets into elastic nanoemulsions by extreme rupturing. *Physical Review E* **2007**, *75*, 041407.

(43) Ayyagari, V. A.; Sumant, A. V. Robust superlubricity with steel surfaces in sliding contacts. 2023; US Patent App. 17/351,817.

(44) Mokshin, A. V.; Barrat, J.-L. Shear induced structural ordering of a model metallic glass. *The Journal of chemical physics* **2009**, *130*.

(45) Landman, U.; Luedtke, W.; Gao, J. Atomic-scale issues in tribology: interfacial junctions and nano-elastohydrodynamics. *Langmuir* **1996**, *12*, 4514–4528.

(46) Thompson, P. A.; Robbins, M. O.; Grest, G. S. Structure and Shear Response in Nanometer-Thick Films. *Israel Journal of Chemistry* **1995**, *35*, 93–106.

(47) Myant, C.; Spikes, H.; Stokes, J. Influence of load and elastic properties on the rolling and sliding friction of lubricated compliant contacts. *Tribology International* **2010**, *43*, 55–63.

(48) Zang, L.; Chen, Y.; Wu, Y.; Liu, H.; Ran, L.; Zheng, Y.; Gao, M.; Ku¨¸cu¨kay, F.; Liu, Y. Tribological performance of Mn3 (PO4) 2 coating and PC/MoS_2 coating in Rolling–Sliding and pure sliding contacts with gear oil. *Tribology International* **2021**, *153*, 106642.

(49) Topolovec-Miklozic, K.; Lockwood, F.; Spikes, H. Behaviour of boundary lubricating additives on DLC coatings. *Wear* **2008**, *265*, 1893–1901.

(50) Boidi, G.; Tertuliano, I. d. S.; Profito, F. J.; De Rossi, W.; Machado, I. F. Effect of laser surface texturing on friction behaviour in elastohydrodynamically lubricated point contacts under different sliding-rolling conditions. *Tribology International* **2020**, *149*, 105613.

(51) Kanazawa, Y.; Sayles, R. S.; Kadiric, A. Film formation and friction in grease lubricated rolling-sliding non-conformal contacts. *Tribology International* **2017**, *109*, 505–518.

(52) Bingley, R.; Buttery, M.; Kelly, G.; Kent, A.; Vortselas, A. Hybrid Lubrication as a Practical Candidate for Space Mechanism Applications. **2021**,

(53) Massocchi, D.; Chatterton, S.; Lattuada, M.; Reddyhoff, T.; Dini, D.; Pennacchi, P. Effect of Friction Reducers with Unreinforced PEEK and Steel Counterparts in Oil Lubrication. *Lubricants* **2023**, *11*, 487.

(54) Björling, M.; Marklund, P.; Larsson, R. On the effect of DLC coating on full film EHL friction. World Tribology Congress: 08/09/2013-13/09/2013. 2013.

(55) Taylor, R. I.; Sherrington, I. Prediction of Friction Coefficients in Mixed Lubrication Regime For Lubricants Containing Anti-Wear and Friction Modifier Additives. *Tribology Online* **2023**, *18*, 185–192.

(56) Baumann, A.; Bertsche, B. Coefficient of friction behavior of gear oils and significance for the meshing process of spur gears: Lubrication for improved properties. *Forschung im Ingenieurwesen* **2022**, 1–11.

(57) Gould, B.; Demas, N. G.; Pollard, G.; Rydel, J. J.; Ingram, M.; Greco, A. C. The effect of lubricant composition on white etching crack failures. *Tribology letters* **2019**, *67*, 1–14.

(58) Guegan, J.; Southby, M.; Spikes, H. Friction modifier additives, synergies and antagonisms. *Tribology Letters* **2019**, *67*, 1–12.

(59) Zhang, J.; Spikes, H. Measurement of EHD friction at very high contact pressures. *Tribology Letters* **2020**, *68*, 42.

(60) Zhang, J.; Ueda, M.; Campen, S.; Spikes, H. Boundary friction of ZDDP tribofilms. *Tribology Letters* **2021**, *69*, 1–17.

(61) Ueda, M.; Wainwright, B.; Spikes, H.; Kadiric, A. The effect of friction on micropitting. *Wear* **2022**, *488*, 204130.

(62) Lundgren, S. M.; Eriksson, K.; Rossenaar, B. Boosting the friction performance of amine friction modifiers with MoDTC. *SAE International Journal of Fuels and Lubricants* **2015**, *8*, 27–30.

(63) Papke, B.; Parthasarathy, P. Tribological Film Formation on Hydrogenated DLC/Steel Contacts From Fully Formulated Automotive Lubricants. International Joint Tribology Conference. 2009; pp 139–141.

(64) Zang, L.; Zhong, Q.; Chen, Y.; Hou, W.; Zhao, B.; Wu, Y. Effect of coating thickness on tribological properties of manganese phosphate conversion coating in different motion conditions. *Tribology International* **2022**, *176*, 107894.

(65) Kanazawa, Y.; De Laurentis, N.; Kadiric, A. Studies of friction in grease-lubricated rolling bearings using ball-on-disc and full bearing tests. *Tribology Transactions* **2020**, *63*, 77–89.

(66) B. Jin, G. Chen, Y. He, C. Zhang, and J. Luo, Lubrication properties of graphene under harsh working conditions. *Materials Today Advances, **2023**, 18,* 10036.

(67) D. Berman and A. Erdemir, Achieving Ultralow Friction and Wear by Tribocatalysis: Enabled by In-Operando Formation of Nanocarbon Films, *ACS nano **2021**, 15*, 18865–18879.

(68) T. Kuwahara, P. Romero, S. Makowski, Volker Weihnacht, G. Moras, and M. Moseler, Mechano-chemical decomposition of organic friction modifiers with multiple reactive centres induces superlubricity of ta-C, *Nature Communications **2019***, 10.

Superlubricity in Solid Lubricated Sliding and Rolling Contacts

Ali Zayaan Macknojia,[†] Mohammad Eskandari,[†] Khalil Omotosho,[†] Maria Cinta Lorenzo Martin,[‡] Aditya Ayyagari,[*,†] and Diana Berman[*,†]

[†]*Department of Materials Science and Engineering, The University of North Texas, Denton, Texas, USA, 76201*

[‡]*Interfacial Mechanics and Materials Group, Applied Materials Division, Argonne National Laboratory, Lemont, IL, USA, 60439*

Supplemental Information

The coating thickness of the deposit was measured using KLI Instruments white light interferometer. A sharp step through the deposit was created using a diamond scribe, and the step height between the substrate and the top of the coating was measured as coating thickness. The average coating thickness was 2.5 ± 0.15 μm as shown in Supplemental Figure 1.

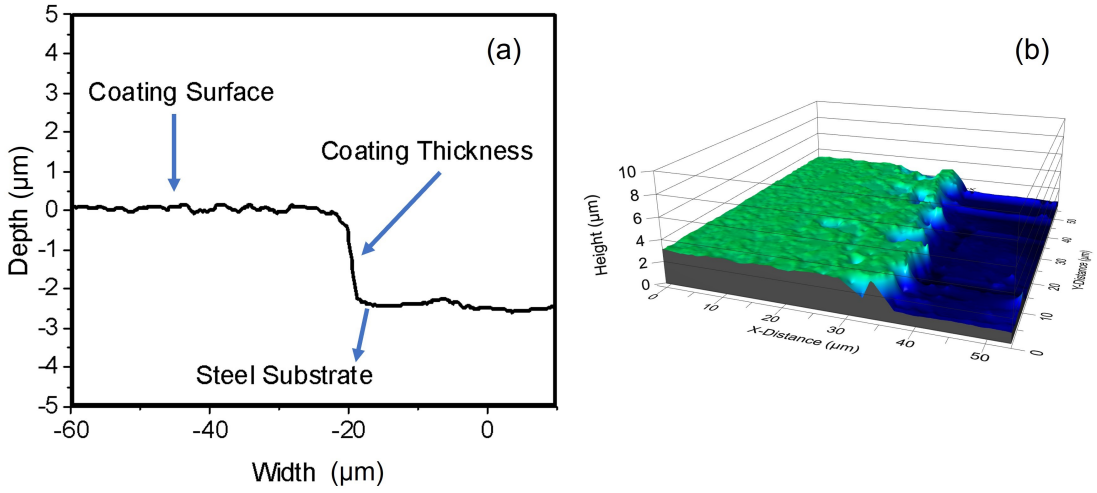

Supplementary Figure S1: *Coating Thickness*

The SEM – EDS elemental maps of the sliding tracks is shown in Supplementary Figure 2. This shows the SEM image of the sliding tracks, as well as the elements detected. It is evident that no underlying steel (Fe signal, yellow) was detected. All other elements remained on the surface. This shows that the coating remained intact and rupture, exposure of substrate did not occur.

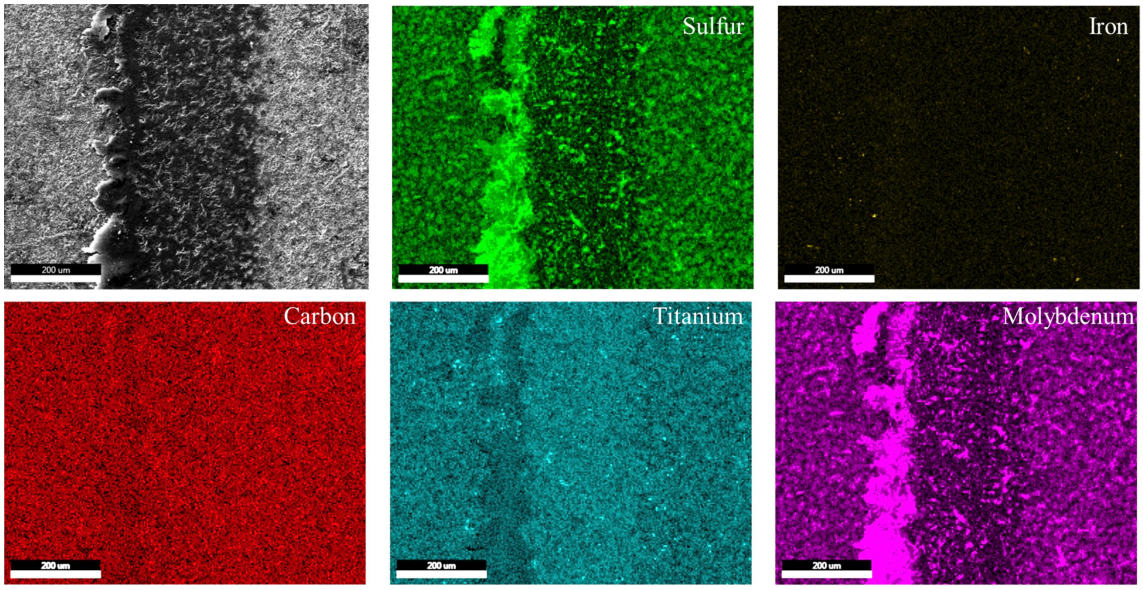

Supplementary Figure S2: *SEM EDS Map showing the elemental distribution*

XPS was acquired using PHI Versaprobe, Al Kα radiation, and the spectra are shown in Supplimentary Figure 3. The peaks show the presence of Ti, Mo, S and Carbon. No oxygen content was observed in the tribolayers.

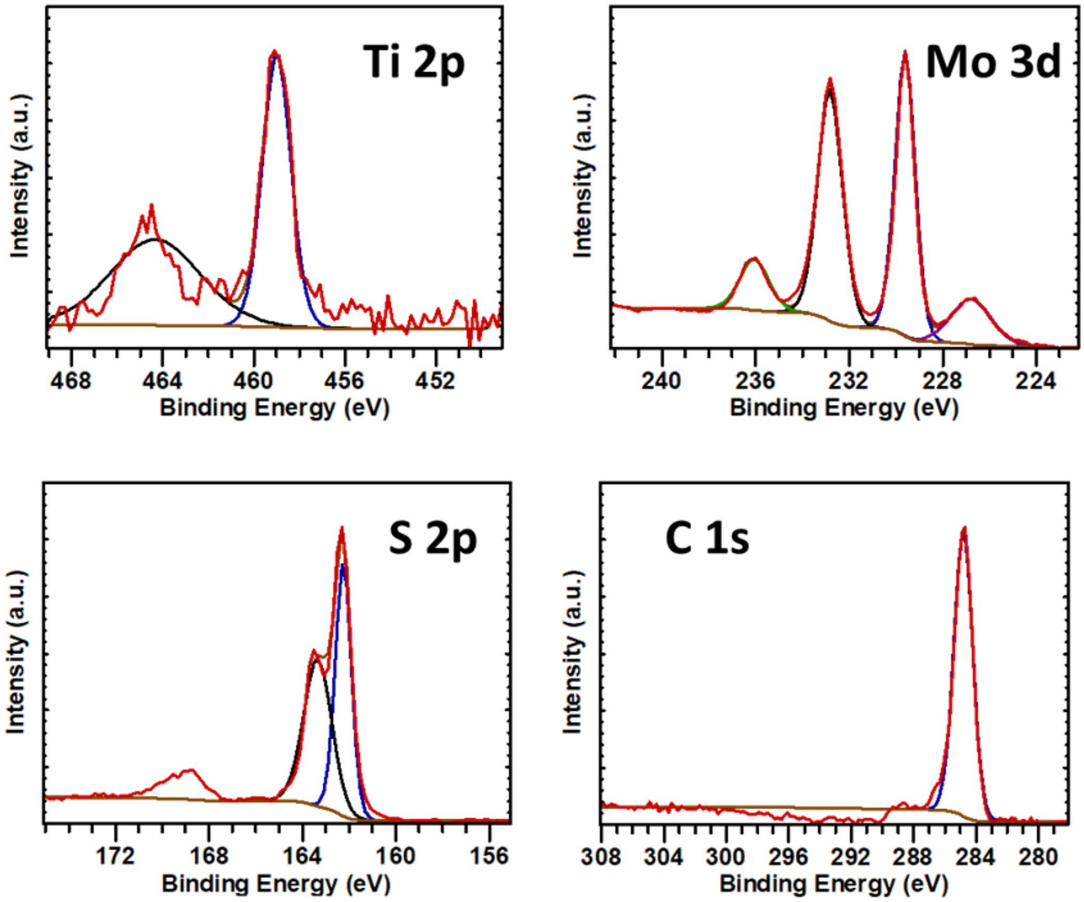

Supplementary Figure S3: *XPS Data*

The hardness and youngs modulus of the coating and wear tracks is shown in Supplimentary Figure 4.

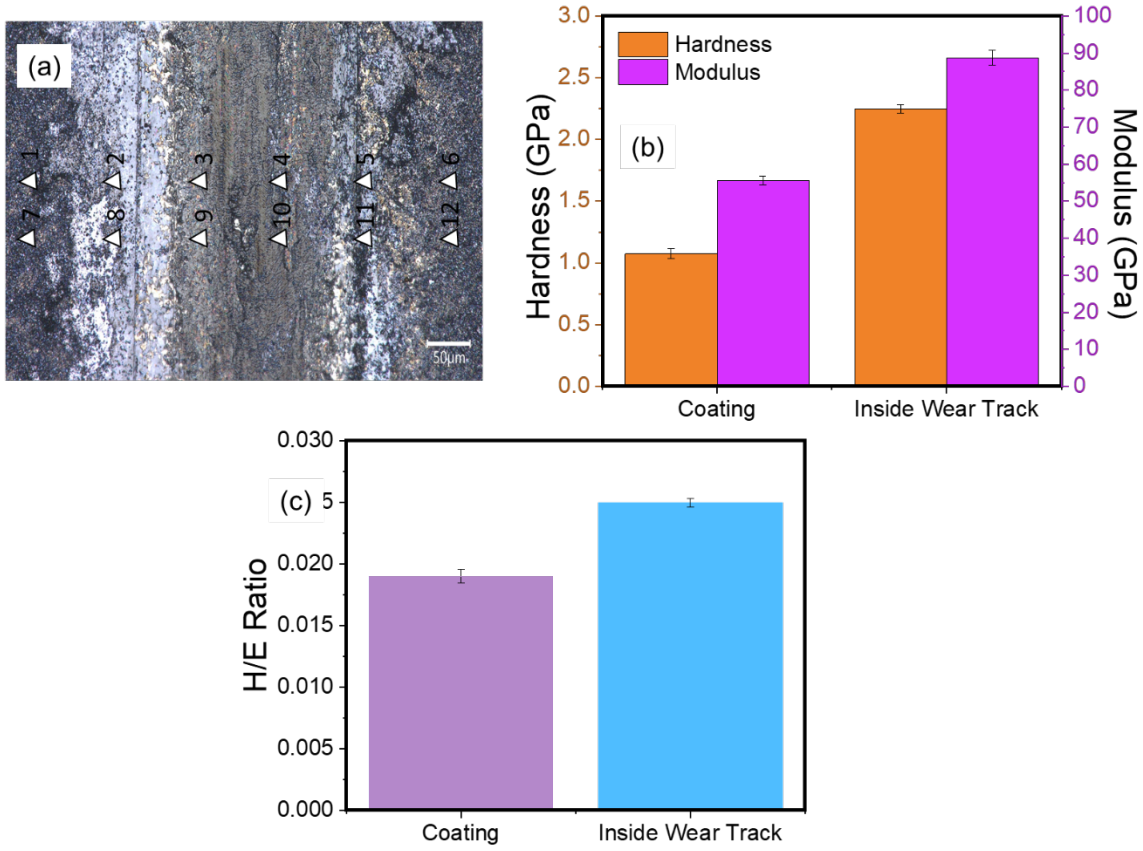

Supplementary Figure S4: *Nanoindentation Data*